

Weighing a galaxy bar in the lens Q2237+0305

Robert Schmidt,^{1*} Rachel L. Webster¹ and Geraint F. Lewis^{2†}

¹ *School of Physics, University of Melbourne, Parkville, Victoria 3052, Australia.*

² *SUNY at Stony Brook, Stony Brook, NY11794-2100, USA.*

ABSTRACT

In the gravitational lens system Q2237+0305 the cruciform quasar image geometry is twisted by ten degrees by the lens effect of a bar in the lensing galaxy. This effect can be used to measure the mass of the bar. We construct a new lensing model for this system with a power-law elliptical bulge and a Ferrers bar. The observed ellipticity of the optical isophotes of the galaxy leads to a nearly isothermal elliptical profile for the bulge with a total quasar magnification of 16^{+5}_{-4} . We measure a bar mass of $7.5 \pm 1.5 \times 10^8 h_{75}^{-1} \mathcal{M}_{\odot}$ in the region inside the quasar images.

Key words: galaxies: fundamental parameters – galaxies: individual: 2237+0305 – galaxies: spiral – gravitational lensing.

1 INTRODUCTION

Gravitational lensing provides a unique way to weigh objects at cosmological distances without any assumption about the connection between light and dark matter. Since the discovery of the first gravitational lens (Walsh, Carswell & Weymann 1979) several gravitational lenses have been found and this method has been used many times to explore the mass distribution of galaxies. In this paper, we model the lens system Q2237+0305 in order to weigh the bar in the lensing galaxy.

The quasar Q2237+0305 ($z_q = 1.695$) was found by Huchra *et al.* (1985) at the centre of an SBb spiral galaxy ($z = 0.0394$) that is situated in the outskirts of the Pegasus II cluster. The quasar was later resolved into four images that are situated around the core of the galaxy within a radius of one arcsecond (Yee 1988; Schneider *et al.* 1988).

Two fundamentally different approaches have been used to model the lensing galaxy. One was to fit a parametric mass profile with several free parameters to the observed quasar image configuration (Kent & Falco 1988); the other to use a model of the light distribution of the galaxy and to fit for the mass-to-light ratio as the single free parameter (Schneider *et al.* 1988; Rix *et al.* 1992). The former approach was naturally much more precise in the reproduction of the observed image geometry due to the greater number of free parameters.

The length scale over which the lensing galaxy influ-

ences a light bundle from the quasar is small compared to the cosmological distances between observer, lens and source. The lens can therefore be treated as a mass sheet at the position of the galaxy. Since the galaxy disk of 2237+0305 is inclined with respect to the sky, elliptical surface mass distributions must be used in the models of this system.

Interestingly, the position angle, counted counterclockwise from north, of the major axis of the elliptical lens models found by Kent & Falco (1988) was about 67° . This is almost parallel to the axis through images C and D and just between the angle of the inclination axis of the galaxy (77° , Yee 1988) and the angle of the bar (39° , also Yee 1988). This situation is shown in figure 1. This was also found by Kochanek (1991) and Wambsganss & Paczyński (1994) who used simple circular mass distributions with an additional quadrupole perturbation. When fitted to the observed image geometry, the direction of the perturbation turned out to be close to the one Kent & Falco (1988) found for their model major axis. More recent investigations by Witt, Mao & Schechter (1995), Kassiola & Kovner (1995) and Witt (1996) obtained the same position angle for the perturbation or major model axis.

On the other hand, the bar shows up prominently in CCD images of the galaxy. It has been noted (Tyson & Gorenstein 1985; Yee 1988; Foltz *et al.* 1992) that it might contribute significantly to the lensing in the system – initially this was actually an aid to explain the lensing effect when only the images A, B and C were known (Tyson & Gorenstein 1985).

The motivation for this paper is the idea that the apparent misalignment of the predicted model major axis and observed galaxy inclination axis as shown in figure 1 is due to the lensing influence of the bar. In section 2 we construct

* Present address: Astrophysikalisches Institut Potsdam, An der Sternwarte 16, 14482 Potsdam, Germany. E-mail: rschmidt@aip.de

† Visiting Astronomer at the University of Melbourne

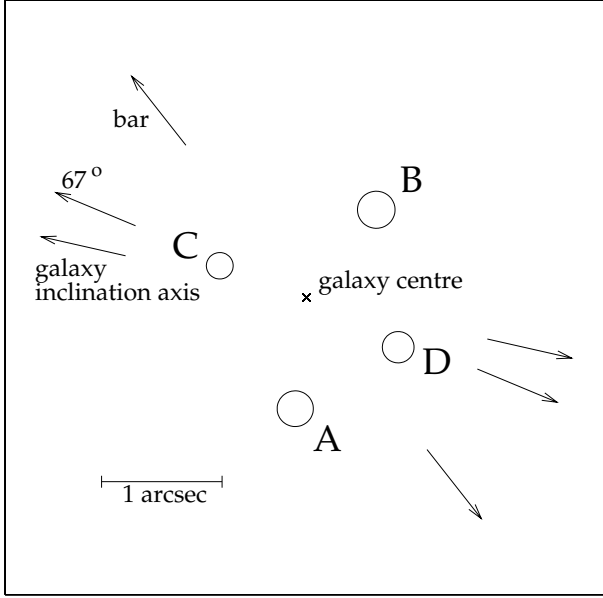


Figure 1. Illustration of the image geometry of Q2237+0305, motivated by figure 1 in Kent & Falco (1988). The images are labelled using the convention by Yee (1988) with positions from Crane *et al.* (1991). The relative areas of the circles correspond to the radio flux ratios from Falco *et al.* (1996). The position of the galaxy centre is indicated with a cross. The long arrows indicate the directions of the galaxy inclination axis and the bar, as well as the position angle of 67° . North is up, East to the left.

and analyse a lensing model that includes the bar component and takes the observed position angle for the inclination axis of the galaxy into account. Section 3 deals with the implications of this model for the bar. In section 4 we finally discuss our results. We use a cosmological model with $H_0 = 75 \text{ h}_{75} \text{ km s}^{-1} \text{ Mpc}^{-1}$, $\Omega = 1$ and $\Lambda = 0$.

2 THEORETICAL MODEL

The lensing model we construct has two components, each with several free parameters. In this section, we introduce the components and determine the values for these that provide the best description of the observations.

2.1 The bulge

Yee (1988) identified three components in the inner part of the galaxy: bulge, disk and bar. In the lensing models for this system, bulge and disk have been represented by just one effective component since there is only limited observational data from the quasar image and galaxy positions to constrain free parameters of the model. For simplicity, we call this composite component ‘bulge’.

Moreover, Kochanek (1991) and Wambsganss & Paczyński (1994) found that the quasar image positions and the galaxy position in this system do not constrain the parameters even of simple lens models. In particular, Wambsganss & Paczyński (1994) showed that for a circular power-law mass distribution with an external shear there is a whole family of models that fit the observations; they discovered that for

this family there is a linear relation between the magnitude of the external shear and the exponent of the mass profile for a vast range of exponents. The shear and the mass exponent are degenerate and one needs more information than only the positions of the quasar images and the galaxy to break this degeneracy. If one uses a two-component galaxy model the shear contributions from the two components will also be degenerate since the resulting shear is degenerate.

One way to get around the shear degeneracy is to use an elliptical mass distribution instead of a circular profile. In this case, the ellipticity-parameter of the mass distribution replaces the shear-parameter as a free parameter of the model. An analogous degeneracy in the ellipticity can then be broken by using the observed ellipticity of the isophotes of the galaxy.

Generalising the approach by Wambsganss & Paczyński (1994), we accordingly modelled the bulge with an elliptical power-law mass distribution with a major axis position angle of 77° . There is some disagreement in the literature on the value of this position angle (for example Rix, Schneider & Bahcall 1992). Fitte & Adam (1994) showed that this is because the position angle of elliptical isophotes is increasingly twisted towards the bar with increasing distance from the galaxy centre. The value we adopted from Yee (1988) is identical with the position angle determined from the galaxy continuum map within a radius of one arcsecond from the galaxy centre (Fitte & Adam 1994) where most of the lensing mass is situated. Let ϵ be the elliptical parameter, so that the ratio b/a of minor and major axis of concentric elliptical shells is

$$\frac{b}{a} = \frac{1 - \epsilon}{1 + \epsilon}. \quad (1)$$

It is useful to express surface mass densities in units of the critical lensing density (Schneider *et al.* 1992) $\Sigma_{\text{crit}} = c^2 D_s / 4\pi G D_d D_{ds}$, where D_s , D_d and D_{ds} are the angular size distances between observer and source, observer and deflector (lens), as well as deflector and source. The surface mass density κ of a power-law elliptical mass distribution in units of Σ_{crit} is given by

$$\kappa(\theta_1, \theta_2) = \frac{E_0}{2\theta_e^\nu}. \quad (2)$$

θ_1 and θ_2 are the coordinates on the sky as measured in a coordinate system oriented with the observed major and minor axis of the bulge. θ_e is the elliptical radius

$$\theta_e = \sqrt{\frac{\theta_1^2}{(1 + \epsilon)^2} + \frac{\theta_2^2}{(1 - \epsilon)^2}}, \quad (3)$$

ν is the power-law exponent of the elliptical mass distribution and E_0 is a constant. In the analysis of our results we use the ellipticity $e = 1 - \frac{b}{a} = \frac{2\epsilon}{1 + \epsilon}$ since this is the value that is usually used in the observations. In Appendix A deflection potential and angles for this mass distribution are described.

2.2 The bar

The light distribution of bars has a well-defined elongated shape, and is non-singular and centrally condensed (Sellwood & Wilkinson 1993). It is not straightforward to determine the true form of bar mass distributions from this,

so that we have to assume a model. Very simple models with these properties of the bar light are the Ferrers profiles (Ferrers 1877). They were used in dynamical studies of bars (Freeman 1966a,b,c; Martinet & de Zeeuw 1988; Sellwood & Wilkinson 1993) since they can be treated analytically. To model the surface mass distribution of the bar of 2237+0305 we used two-dimensional Ferrers profiles of the form

$$\kappa(\theta_1, \theta_2) = \begin{cases} \kappa_c (1 - \frac{\theta_1^2}{a^2} - \frac{\theta_2^2}{b^2})^\lambda & \text{if } \frac{\theta_1^2}{a^2} + \frac{\theta_2^2}{b^2} \leq 1 \\ 0 & \text{otherwise} \end{cases} \quad (4)$$

In this equation, θ_1 and θ_2 are the coordinates on the sky as measured in a coordinate system oriented with the observed major and minor axis of the bar. λ is a real number, κ_c is the central surface density in units of the critical lensing density Σ_{crit} defined in section 2.1 and a , b are the semi-major respectively semi-minor axis of the bar.

In the analysis we restricted ourselves to moderate exponents $\lambda = 0.5, 1$ and 2 . The deflection potential and angles for integer values of λ can be calculated analytically as described in Appendix B. For $\lambda = 0.5$ the profiles were constructed through the numerical superposition of many elliptical slices of constant density ($\lambda = 0$) and different size (Schramm 1994).

2.3 The effect of shear

The lensing influence of the bar can be understood by considering a system with two shear tensors with shear directions as shown in figure 1 for galaxy inclination axis and bar (see Schneider, Ehlers & Falco (1992) for the definition of the shear tensor). The resulting shear tensor can be found by adding up the single tensors and the resulting shear direction is determined by the shear ratio of the two components.

A source almost directly behind the core of the lensing galaxy appears lensed with four of the five images in a cross formation aligned with the axes parallel and perpendicular to the resulting shear direction, while the fifth is seen in the centre (Schneider *et al.* 1992, p252). In the case of 2237+0305, the major axis position angle as found by the one-component lens models (67°) can be interpreted to be this resulting shear direction, which almost coincides with the axis through images C and D. The axis through images C and D has effectively been twisted away from the galaxy inclination axis by the bar.

In figure 2 this twisting is illustrated by plotting the critical lines, caustics and image positions of two barred lenses with identical source positions. The caustics are the lines in the source plane that separate regions of different image multiplicity. The critical lines are the corresponding lines in the lens plane where pairs of images are created or destroyed (Schneider *et al.* 1992).

In this figure, the first lens has a weak bar that barely changes the elliptical shape of the bulge's critical line or the corresponding diamond shape of the caustic. The other bar is significantly more massive; it warps the shape of these structures and shifts the image positions.

2.4 Detailed modelling

Our barred galaxy model has ten adjustable parameters. These are the positions of the galaxy and the source plus

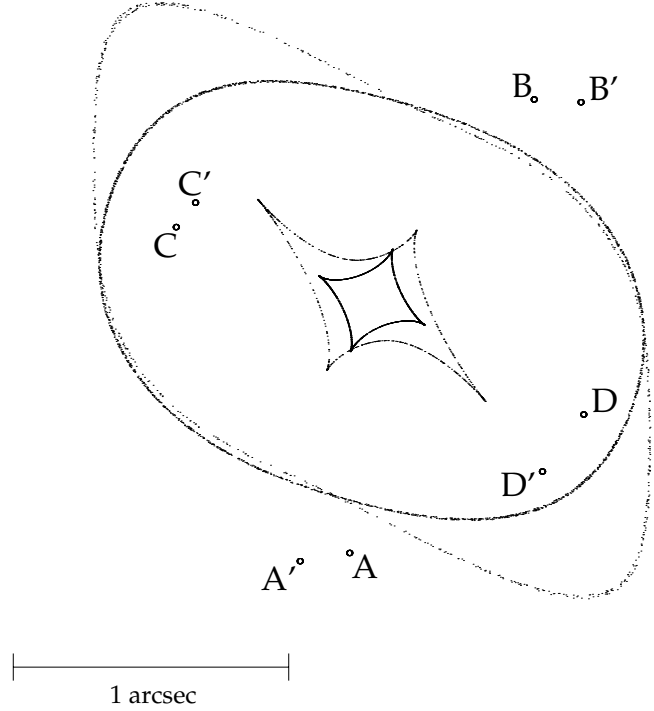


Figure 2. Illustration of the effect of a strong bar. Assuming identical source positions, the diamond-shaped caustics, the corresponding critical curves and the image positions are plotted for two different lenses. The smaller caustic and the almost elliptical critical curve belong to a model with a $\nu = 1$ power-law bulge and a $\lambda = 2$ Ferrers bar that was fitted to the observed parameters of Q2237+0305. The positions of the images created by this model are labelled with unprimed letters as in figure 1. In this model, the bulge mass inside the ring of images is about 20 times larger than the bar mass (see table 1). The caustic and the critical curve transform into the two elongated curves if the mass of the bar inside the ring of images is increased to half the mass of the bulge, while the bulge mass is kept fixed. The images are shifted by the more massive bar to the positions labelled with the primed letters.

the constant E_0 , the ellipticity e and the exponent ν for the bulge as well as the bar mass normalisation κ_c , the semi-minor axis b and the exponent λ for the bar. This number can be reduced by two if the observed ellipticity of the bulge and only fixed values for λ are used. For the length of the semi-major axis of the bar we used the observed value of $a \approx 9$ arcsec (taken from the figures in Yee 1988 or Irwin *et al.* 1989). The lens effect is insensitive to the precise value of a because a is much larger than the radius of the ring of images (≈ 1 arcsec). The length of the semi-minor axis must, however, remain a free parameter of the model since it is comparable to this radius, but not known well enough ($b \approx 1 - 2$ arcsec, see section 3).

There are ten observational constraints the system imposes upon theoretical models. These are the coordinates of the four observed quasar images and the galaxy centre. The positions for the images and galaxy centre were taken from Crane *et al.* (1991). These positions have been determined from *Hubble Space Telescope* (HST) observations and have quoted measurement errors of $0''.005$. In general, the ratios of the fluxes of the different images of a gravitational lens also provide good constraints for a model. Unfortunately, in

the case of Q2237+0305 the lightcurves from Corrigan *et al.* (1991) or Østensen *et al.* (1996) clearly show that all optical image fluxes are subject to flux variations due to microlensing of the quasar light from the stars in the lensing galaxy. In addition, the light from the quasar is non-uniformly dust reddened during the passage through the galaxy. The fluxes were, therefore, neglected in the modelling procedure. We will, however, compare the model predictions with the recently measured radio flux densities by Falco *et al.* (1996).

Let $\vec{\theta}_k, \vec{\theta}_g$ be the positions on the sky the model predicts for quasar images and the galaxy centre and $\vec{\theta}_{ko}, \vec{\theta}_{go}$ the observed positions with their positional uncertainties σ_k, σ_g . To find the best fit model, the expression

$$\chi^2 = \sum_{k=1}^4 \frac{(\vec{\theta}_k - \vec{\theta}_{ko})^2}{\sigma_k^2} + \frac{(\vec{\theta}_g - \vec{\theta}_{go})^2}{\sigma_g^2} \quad (5)$$

(Wambsganss & Paczyński 1994) was minimised through variation of the model parameters using a multidimensional minimisation routine (direction set or downhill simplex methods according to Press *et al.* 1992).

In order to find an estimator for the separations $\vec{\theta}_k - \vec{\theta}_{ko}$ between modelled and observed images for the first term on the right hand side of Equation (5), we used the method by Kochanek (1991); the separations between an optimally weighted source position and the positions in the source plane where the observed image positions are mapped to by a given lens model are propagated back into the lens plane.

2.5 Analysis

For a nearly circularly symmetric lens with a source almost in the origin, it follows from Newton's theorem in two dimensions (Foltz *et al.* 1992; Schramm 1994) that the mass inside the circle of images is approximately given by the separation $\Delta\theta$ of the images at opposite ends of the cross via

$$M = \frac{c^2}{16G} \frac{D_d D_s}{D_{ds}} (\Delta\theta)^2 \quad (6)$$

(see for example Narayan & Bartelmann 1996). The galaxy 2237+0305 is situated relatively close to us at an angular size distance $D_d = 0.15 \text{ h}_{75}^{-1} \text{ Gpc}$, so that $D_{ds}/D_s \approx 1$. The separations of the quasar images are $\Delta\theta \approx 1.8 \text{ arcsec}$, so that we get $M \approx 1.5 \times 10^{10} \text{ h}_{75}^{-1} \mathcal{M}_\odot$. This value was also found in previous models for this system (Rix *et al.* 1992: $1.44 \pm 0.03 \times 10^{10} \text{ h}_{75}^{-1} \mathcal{M}_\odot$, Wambsganss & Paczyński 1994: $1.48 \pm 0.01 \times 10^{10} \text{ h}_{75}^{-1} \mathcal{M}_\odot$). The other value theoretical models for 2237+0305 agreed on was the resulting shear direction of $\approx 67^\circ$.

In our barred lens model, the bulge acts as the main lensing mass and the bar as a perturbation; for a given ellipticity e or exponent ν , the bulge parameter E_0 and hence the bulge mass do not change very much for different λ -bar models. In fact, experiments with different bar masses as in figure 2 showed that for similar masses of bulge and bar inside the quasar images the cruciform image symmetry gets skewed. Models with a strong bar thus cannot reproduce a symmetric image geometry as in Q2237+0305. In order to explore the effect of λ on the models, we used fixed values $\lambda = 0.5, 1$ and 2 .

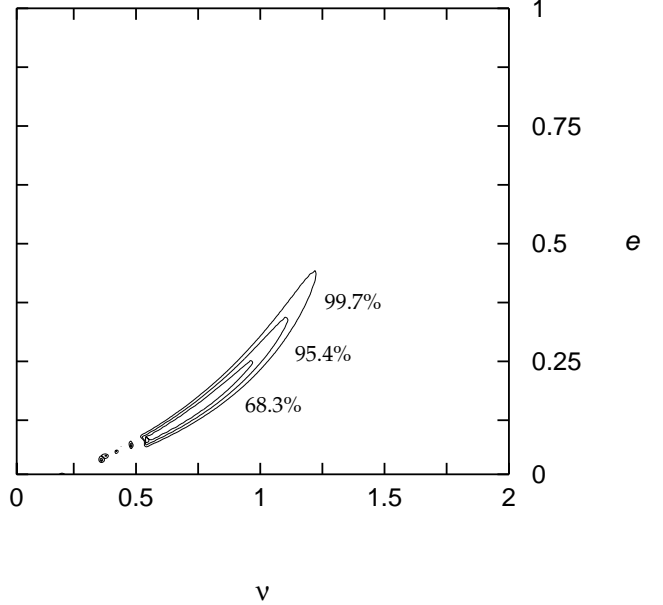


Figure 3. Contour plot of confidence regions in the parameter space of bulge exponent ν and ellipticity e . The indicated contours contain 68.3%, 95.4% and 99.7% of normally distributed models around the minimum of χ^2 .

Besides E_0 and λ , the parameter space of e, ν, κ_c and b had to be examined. We first scanned the parameter space of e and ν while leaving κ_c and b as free parameters. In figure 3 a contour plot of the confidence regions that contain 68.3%, 95.4% and 99.7% of normally distributed models around the minimum of χ^2 (Press *et al.* 1992) in the parameter space of ν and e is shown. Only the plot for $\lambda = 2$ is presented; the cases with $\lambda = 0.5$ and $\lambda = 1$ are very similar. The parameter space was scanned with a stepsize of 0.02 for ν and 0.01 for e . For every point the best parameters were determined through minimisation and a χ^2 -value was computed. The best fit models lie in a long valley that extends up to $\nu \approx 1.25$. The unclear structure at the lower end of the valley for $\nu \leq 0.5$ and $e \leq 0.1$ is due to numerical effects. Detailed investigation shows that the valley continues towards smaller ν , becoming shallower. The models in this region, with low e and ν , are similar to circular disks with constant surface mass density and are not examined here because they do not represent realistic galaxy models.

The external-shear models by Wambsganss & Paczyński (1994) yielded no constraints on their circular mass distributions for the whole range of parameters from $\nu = 0.07$ to $\nu = 2$. The smaller allowed range for ν in figure 3 shows that the ellipticity does not allow the same kind of freedom as the shear. For high ellipticities of the power-law bulges, the quasar image geometry cannot be reproduced anymore.

In figure 4 the total mass, the bulge mass, and the bar mass inside a circle of 0.9 arcsec as well as the semi-minor axis b and the total magnification μ along the valley of best fits around the $\nu = 1$ profile are shown for $0.75 \leq \nu \leq 1.3$ and the three values of λ . The plots for different λ only differ noticeably in their semi-minor axis predictions. Beginning with $\nu \approx 1.2$ the minimisation produces numerical noise at the upper end of the valley from figure 3 since the fits get worse.

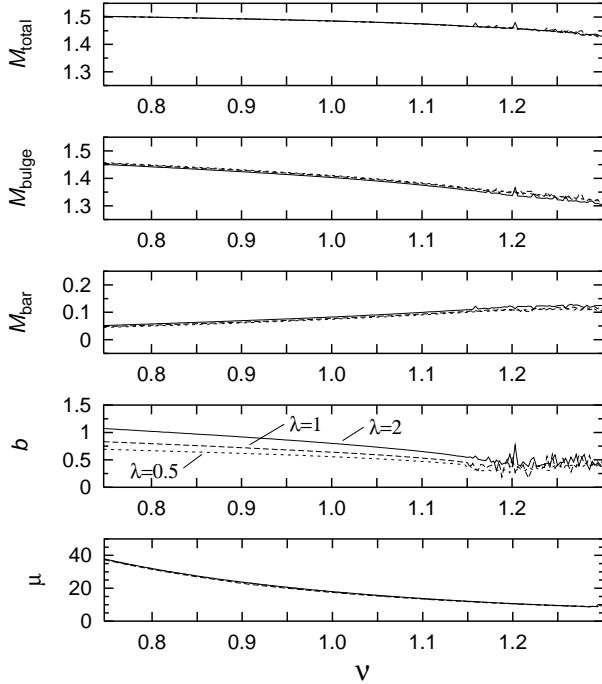


Figure 4. Model parameters along the valley of best fits. Plotted against ν are the total mass and the masses of bulge and bar inside a circle of 0.9 arcsec in $10^{10} h_{75}^{-1} M_{\odot}$ as well as the semi-minor bar axis b in arcsec and the total magnification μ . Different line styles have been used for different values of λ as indicated in the b - ν panel.

It can be seen that the total mass of the model inside a circle of 0.9 arcsec is almost constant. The constituent masses of the bar and the bulge exhibit a dependence on ν . It can be interpreted that the bar mass increases with ν in order to counter the increased contribution of the bulge to the resulting shear due to the increase of e , and hence the bulge mass decreases in order to conserve the mass inside 0.9 arcsec given by equation (6). The magnification drops strongly with increasing ν , which was also observed by Wambsganss & Paczyński (1994).

As motivated in the introduction, we chose the model from the family of best models in figure 3 that exhibits the observed ellipticity of the bulge. The ellipticity has been measured by Racine (1991) to be $e = 0.31 \pm 0.02$, in agreement with the results from the continuum map by Fitte & Adam (1994). This range of ellipticities is encompassed by the range $\nu = 1.05 \pm 0.1$ of bulge exponents. We use this region of allowed bulge models to determine the uncertainties of the predictions of models with different bars.

From all possible values for ν and the three bar models we obtain an estimate of the total mass inside a circle of 0.9 arcsec of $1.49 \pm 0.01 \times 10^{10} h_{75}^{-1} M_{\odot}$. This is consistent with the estimate and the results from the literature given at the beginning of this section. In a review, Narayan & Bartelmann (1996) mention only two cases of gravitational lenses in which it has been possible to constrain the radial distribution of the lens galaxy. Both models are based on singular elliptical or nearly elliptical profiles. For MG 1654+134,

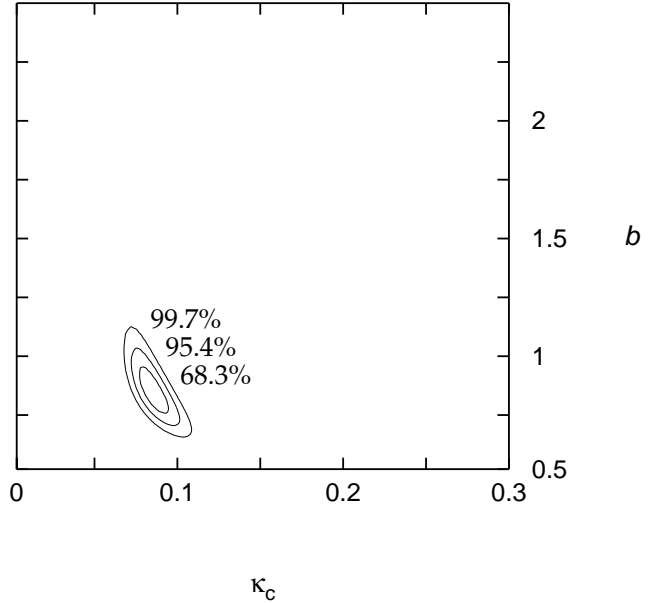


Figure 5. Contour plot of confidence regions in the parameter space of bar normalisation κ_c and semi-minor axis b (in arcsec) for a bulge exponent $\nu = 1.05$, ellipticity $e = 0.31$ and bar exponent $\lambda = 2$. The indicated contours contain 68.3%, 95.4% and 99.7% of normally distributed models around the minimum of χ^2 .

Kochanek (1995) obtained $\nu = 1.0 \pm 0.1$, and for QSO 0957+561, Grogin & Narayan (1996) obtained $\nu = 1.1 \pm 0.1$. The predictions of our model for the bulge are in good agreement with these values.

In table 1, the model parameters for the different values of λ and the uncertainties due to the uncertainty in ν are shown. The χ^2 -values from equation (5) have been divided by the number of degrees of freedom, giving a measure of the quality of the fit. The number of degrees of freedom is the number of constraints minus the number of free parameters; here we have three degrees of freedom since e , ν and λ are fixed.

The value for the total magnification predicted from the $\nu = 1.05$ model is about half the value found by Wambsganss & Paczyński (1994) for their $\nu = 1$ circular power law profile with an external shear. This illustrates that the use of an elliptical mass distribution drastically changes the predictions of the model; a similar discrepancy is apparent for the time-delays. Note that $\mu_{\text{total}} \approx \frac{3}{\epsilon} = 16.7$ with $\epsilon = 0.18$ (corresponds to $e = 0.31$, see section 2.1) as derived for a $\nu = 1$ power-law lens with small ϵ and a source in the origin by Kassiola & Kovner (1993). In contrast to the non-singular mass models by Kent & Falco (1988) our lens models do not produce a fifth image in the centre due to the central singularity of the mass distribution. The predicted source positions are very similar to the ones by Kent & Falco.

The remaining parameter space of the bar models is illustrated in figure 5. Similar to figure 3, the contours of the confidence regions of normally distributed models around the minimum of χ^2 in the parameter space of κ_c and b are shown for the model with $\nu = 1.05$, $e = 0.31$ and $\lambda = 2$. The parameter space was scanned with a stepsize of 0.003 in κ_c and 0.025 arcsec in b . The bar parameters are well constrained at the bottom of a steep boomerang-shaped valley.

Table 1. Model Parameters for Q2237+0305 for three values of the bar exponent λ and the bulge exponent ν . The columns for $\lambda = 0.5, 1.0$ and 2.0 are indicated. Each table entry contains the value for $\nu = 1.05$ and the differences to the corresponding values for $\nu = 1.15$ (upper index) and 0.95 (lower index). Only one value is given for a line if the differences between the bar models are below the rounding precision. χ^2 is divided by three, the number of degrees of freedom. E_0 , b and the source position (β_1, β_2) are given in arcsec. μ_{total} is the total magnification, μ_{ij} are the relative magnification ratios between the images. Δt_{ij} are the relative time-delays between the images in h_{75}^{-1} hours. $M_{\text{bulge}}(< 0.9'')$ and $M_{\text{bar}}(< 0.9'')$ are the masses of bulge and bar inside a circle of 0.9 arcsec and $M_{\text{bar,total}}$ is the total mass of the bar. Masses are given in $10^{10} \text{h}_{75}^{-1} \mathcal{M}_{\odot}$. The semi-major bar axis was assumed as $a = 9$ arcsec. The VLA flux ratios are the 3.6cm radio flux ratios measured by Falco *et al.* (1996).

λ	0.5	1.0	2.0	VLA flux ratios
$\chi^2/3$		$2.1^{+1.3}_{-0.8}$		
E_0		$0.81^{+0.09}_{-0.09}$		
e		$0.31^{+0.07}_{-0.06}$		
κ_c	$0.074^{+0.022}_{-0.014}$	$0.079^{+0.021}_{-0.016}$	$0.085^{+0.023}_{-0.017}$	
b	$0.58^{+0.06}_{-0.04}$	$0.67^{+0.07}_{-0.06}$	$0.85^{+0.10}_{-0.08}$	
β_1		$-0.063^{+0.010}_{-0.009}$		
β_2		$-0.014^{+0.003}_{-0.001}$		
μ_{total}	$15.6^{+3.5}_{-4.8}$	$16.0^{+3.6}_{-5.0}$	$16.2^{+3.6}_{-5.0}$	
μ_{BA}	$1.12^{+0.02}_{-0.01}$	$1.08^{+0.03}_{-0.04}$	$1.04^{+0.03}_{-0.03}$	1.08 ± 0.27
$-\mu_{\text{CA}}$	$0.62^{+0.04}_{-0.04}$	$0.61^{+0.01}_{-0.01}$	$0.60^{+0.02}_{-0.02}$	0.55 ± 0.21
$-\mu_{\text{DA}}$	$1.26^{+0.07}_{-0.06}$	$1.26^{+0.01}_{-0.01}$	$1.24^{+0.02}_{-0.02}$	0.77 ± 0.23
$-\Delta t_{\text{BA}}$		$2.0^{+0.4}_{-0.3}$		
Δt_{CA}		$16.2^{+2.7}_{-4.4}$		
Δt_{DA}		$4.9^{+1.0}_{-0.8}$		
$M_{\text{bulge}}(< 0.9'')$	$1.42^{+0.02}_{-0.01}$	$1.42^{+0.02}_{-0.01}$	$1.41^{+0.01}_{-0.02}$	
$M_{\text{bar}}(< 0.9'')$	$0.07^{+0.01}_{-0.01}$	$0.07^{+0.01}_{-0.01}$	$0.08^{+0.01}_{-0.01}$	
$M_{\text{bar,total}}$	$0.47^{+0.07}_{-0.06}$	$0.43^{+0.06}_{-0.06}$	$0.39^{+0.05}_{-0.05}$	

Table 2. Local lensing parameters at the positions of the quasar images. The values have been determined with a $\lambda = 1$ bar, but they are identical for $\lambda = 0.5$ and 2 within ± 0.01 . Each table entry contains the value for $\nu = 1.05$ and the differences to the corresponding values for $\nu = 1.15$ (upper index) and 0.95 (lower index).

Image	κ	γ
A	$0.36^{+0.07}_{-0.07}$	$0.40^{+0.03}_{-0.03}$
B	$0.36^{+0.06}_{-0.06}$	$0.42^{+0.03}_{-0.03}$
C	$0.69^{+0.01}_{-0.01}$	$0.71^{+0.09}_{-0.09}$
D	$0.59^{+0.03}_{-0.02}$	$0.61^{+0.06}_{-0.06}$

The surface mass density κ in units of the critical density and the local shear γ at the positions of the images are given in table 2. The values for $\nu = 0.95$ and 1.05 are similar to what one gets for a circular $\nu = 1$ power-law mass distribution (singular isothermal sphere) with a mixture of internal and external shear (Kochanek 1991; Witt & Mao 1994). It can be taken from tables 1 and 2 that a change of λ does not cause a measurable change of observable quantities except for the semi-minor axis of the bar; the uncertainty

of the model parameters is dominated by the uncertainty of the bulge ellipticity e /exponent ν .

3 PROPERTIES OF THE BAR

The width of the bar has not been measured previously. In figure 1 of their paper, Irwin *et al.* (1989) present a contour plot of the galaxy where the bar has been separated from the disk. In this plot, the bar appears about 18 arcsec long, but only $\approx 2 - 4$ arcsec wide. It is just the less well-known minor axis that enters the lensing model since the quasar images are situated in the centre of the galaxy. In their image analysis Irwin *et al.* subtracted structure from their image that is smooth on scales of $\approx 5 - 10$ arcsec. This procedure removed the galaxy disk very efficiently, but, being long as well as thin, the bar shown in their figure 1 could also be affected by this procedure.

A different approach to obtain the light distribution of the bar was pursued by Schmidt (1996). Using a *Hubble Space Telescope (HST)* I-band image taken with the Planetary Camera prior to the first servicing mission (Westphal 1992), the galaxy was decomposed into bulge, disk and bar with analytical profiles that have been convolved with the

point-spread function of the telescope. Exponential profiles (Andredakis & Sanders 1994) were fitted to bulge and disk. After these components were removed from the image, the bar and the spiral arms remained. The bar light distribution could be fit with a $\lambda = 2$ Ferrers profile with $a = 9.5 \pm 1.0$ arcsec and $b = 1.0 \pm 0.3$ arcsec. This light model can be combined with the mass model for $\lambda = 2$ from table 1 due to the similar value for b ; the I-band mass-to-light ratios of these model components inside a circle of 0.9 arcsec are given by $\mathcal{M}/L_I \approx 4.8 h_{75}$ for bulge plus disk and $\mathcal{M}/L_I \approx 5.0 h_{75}$ for the bar. The bar mass detected with gravitational lensing and the bar light in the I-band in this model both constitute a 5% fraction of the total mass respectively light inside 0.9 arcsec.

This result is, however, dependent on the bulge model. For a de Vaucouleurs–bulge (de Vaucouleurs 1948), a $\lambda = 0.5$ Ferrers profile fitted the bar light much better with a similar value for a , but a much larger value $b = 3.1 \pm 0.9$ arcsec which cannot be combined with the lensing model from table 1 since b is very different. The unrefurbished *HST* point spread function inhibited a clear distinction between the quality of fit of these different bulge models, so that the question about the minor bar axis is not decided yet.

A value of $b \geq 1$ arcsec could in connection with the values for b in table 1 be taken as evidence in favour of steeper bar models, $\lambda \geq 2$. There is observational evidence from the light distributions of real bars for more boxy mass distributions (Freeman 1996), so that it has to be ascertained that this result is not a relic of the approximation of the bar with an elliptical shape. At the positions of the quasar images, however, an ellipse is a good approximation of a box due to the large semi-major axis of the bar, $a \approx 9$ arcsec. A lensing model with a steeper Ferrers profile with $\lambda = 10$ leads to a larger bar with $b = 2.0$. This indicates that a measurement of the extent of the bar could in principle constrain the mass distribution of the bar. If one wants to use this method, high resolution images with small seeing have to be used since an accuracy of the bar width on the order of tenths of an arcsecond is needed.

4 DISCUSSION

In this paper we have presented a barred galaxy model for the gravitational lens 2237+0305. We used a power-law elliptical mass distribution for the bulge and chose the model for which the observed ellipticity is predicted. It turned out that this model has an exponent close to unity, which is compatible with other determinations of lens mass profiles through gravitational lensing (Kochanek 1995; Grogin & Narayan 1996). The bar represents a small perturbation of the deflection field of the bulge of the galaxy, amounting to $7.5 \pm 1.5 \times 10^8 h_{75}^{-1} \mathcal{M}_\odot$ or about 5% of the bulge mass in the critical region inside the quasar images.

The relative magnifications our model predicts for the quasar images can be compared with the 3.6cm radio flux ratios published by Falco *et al.* (1996). Their results are also given in table 1. Falco *et al.* argue that it is unlikely that the radio flux densities are variable from microlensing due to the larger size of the radio emitting region as compared to the optical continuum emitting region, although they cannot completely rule out microlensing as an important effect in

the radio. If microlensing is not important, the model magnification ratios should be identical to these measured flux ratios. It can be seen that only the ratio μ_{DA} between images D and A is not compatible with their results although no effort was made to fit the flux ratios.

In order to find out more about the discrepancy of the ratio μ_{DA} between observation and model one has to make the relatively large error bars from Falco *et al.* smaller through longer radio observation of the object. Unfortunately, Q2237+0305 has a radio flux density of only ≈ 1 mJy (Falco *et al.* 1996), so that radio observations of this object are very time-consuming; Falco *et al.* observed for 11 hours of which only five could be used eventually due to weather conditions.

To get additional, independent arbiters for the model, it would be very helpful to measure the time-delays in this system. Since the time-delays are of the order of several hours, this has to be done in a wavelength domain where the necessary intra-day variability is likely to occur for a radio-quiet quasar, for example in the x-ray regime as proposed by Wambsganss & Paczyński (1994). Also, monitoring in the radio would show if the quasar image flux densities vary at these frequencies. Unless we learn more about the radio flux densities and the time delays, it is not possible to decide whether or not it is microlensing that causes the low magnification of image D. In the optical, image D has always been the faintest quasar image. In fact, in the first resolved image of the quasar, image D was not visible at all (Tyson & Gorenstein 1985). There is also spectroscopic evidence from optical data that image D is undergoing demagnification (Lewis *et al.* 1996).

If image D is in fact microlensed in the radio, the consequences are interesting. The scale size of the radio region could be less than the characteristic scale of the caustic network. Alternatively, the radio source could have an asymmetric structure like a jet that would have differing microlensing properties for different paths of the microlenses across the source.

Yet another way to significantly change the radio flux density of image D would be a globular cluster or black hole (Lacey & Ostriker 1985) with a mass of about $10^6 \mathcal{M}_\odot$ in the halo of the lensing galaxy that is situated close to image D. An object of this mass would magnify or demagnify the radio image of the quasar, depending on its location with respect to the direction of the local shear. This effect, the perturbation of lens models by $10^6 \mathcal{M}_\odot$ objects, has recently been treated by Mao & Schneider (1997). With this, we can estimate that a surface mass density of globular clusters or black holes of approximately $0.04 \Sigma_{\text{crit}}$ (Σ_{crit} is defined in section 2.1) or $470 h_{75} \mathcal{M}_\odot/\text{pc}^2$ is needed to observe a demagnification of image D by 40% or more with a probability of 20%. Higher surface mass densities would make it more likely. This is much more than the globular cluster surface mass density of about $1 \mathcal{M}_\odot/\text{pc}^2$ seen in our Galaxy within 5 kpc of the Galactic centre (Mao & Schneider 1997). It thus seems unlikely that the demagnification is due to a globular cluster.

The question of the existence of such a massive object near image D could be solved with a method that was proposed by Wambsganss & Paczyński (1992). They showed that these objects would bend or even create holes in the radio maps of milliarcsecond jets of gravitationally lensed

quasars. If we could observe extended structure of the images of the radio-weak Q2237+0305, features due to globular cluster or black hole lensing could be easily identified because they would not be seen in the other gravitationally lensed images of the quasar.

It has recently been suggested (Keeton, Kochanek & Seljak 1996; Witt & Mao 1997) that a strong lensing perturbation is necessary for a number of lenses in addition to an elliptical mass distribution in order to model the observed image geometry. In our model for Q2237+0305, the additional perturbation from the bar is small, but the system is, nevertheless, unique in that we can see the perturbing agent. For the lens systems mentioned in these papers, the better fit for the models was obtained with an additional external shear. We saw, when we compared our results with Wambsganss & Paczyński (1994), that the predictions for magnifications or time-delays from shear models differ by up to a factor of two from the predictions from elliptical mass deflectors. If one wants to get lensing models with reliable predictions for magnifications or time-delays, the necessary perturbations will ultimately have to be generated in the models by mass components like dark matter haloes (Keeton *et al.* 1996) or bars.

ACKNOWLEDGMENTS

We thank Hans-Jörg Witt, Joachim Wambsganss and the anonymous referee for their comments on the manuscript. RWS gratefully acknowledges support by a Melbourne University Postgraduate Scholarship, an Australian Overseas Postgraduate Research Scholarship and by the Studienstiftung des deutschen Volkes. This research was supported in part by the Deutsche Forschungsgemeinschaft (DFG) under Gz. WA 1047/2-1.

REFERENCES

- Andredakis Y. C., Sanders R. H., 1994, MNRAS, 267, 283
 Corrigan R. T., *et al.*, 1991, AJ, 102, 34
 Crane P., *et al.*, 1991, ApJ, 369, L59
 de Vaucouleurs G., 1948, Ann. d'Ap, 11, 247
 Falco E. E., Lehár J., Perley R. A., Wambsganss J., Gorenstein M. V., 1996, AJ, 112, 897
 Ferrers N. M., 1877, Quart. J. Pure Appl. Math., 14, 1
 Fitte C., Adam G., 1994, A&A, 282, 11
 Freeman K. C., 1966a,b,c, MNRAS, 133, 47 & MNRAS, 134, 1, 15
 Freeman K. C., 1996, in Barred Galaxies, ed. R. Buta, D. A. Crocker and B. G. Elmegreen, Astronomical Society of the Pacific Conference Series, San Francisco, p1
 Foltz C. B., Hewett P. C., Webster R. L., Lewis G. F., 1992, ApJ, 386, L43
 Grogin N. A., Narayan R., 1996, ApJ, 464, 92
 Huchra J., Gorenstein M., Horine E., Kent S., Perley R., Shapiro I. I., Smith G., 1985, AJ, 90, 691
 Irwin M. J., Webster R. L., Hewett P. C., Corrigan R. T., Jedrzejewski R. I., 1989, AJ, 98, 1989
 Kassiola A., Kovner I., 1993, ApJ, 417, 450
 Kassiola A., Kovner I., 1995, MNRAS, 272, 363
 Keeton C. R., Kochanek C. S., Seljak U., 1996, submitted; preprint astro-ph/9610163
 Kent S. M., Falco E. E., 1988, AJ, 96, 1570
 Kochanek C. S., 1991, ApJ, 373, 354
 Kochanek C. S., 1995, ApJ, 445, 559
 Kormann R., Schneider P., Bartelmann M., 1994, A&A, 284, 285
 Lacey C. G., & Ostriker J. P., 1985, ApJ, 299, 633
 Lewis G. F., Irwin M. J., Hewett P. C., Foltz C. B., 1996, in Astrophysical Applications of Gravitational Lensing, ed. C. S. Kochanek & J. N. Hewitt, Kluwer, Dordrecht, p241
 Mao S., & Schneider P., 1997, talk held at the Jodrell Bank workshop on Golden Lenses; preprint astro-ph/9707187
 Martinet L., de Zeeuw T., 1988, A&A, 206, 269
 Narayan R., Bartelmann M., 1996, 'Lectures on Gravitational Lensing', held at the 1995 Jerusalem Winter School; preprint astro-ph/9606001
 Østensen R., *et al.*, 1996, A&A, 309, 59
 Pfenniger D., 1984, A&A, 134, 373
 Press W. H., Teukolsky S. A., Vetterling W. T., Flannery B. P., 1992, Numerical Recipes in C, 2nd edition (Cambridge University Press, Cambridge)
 Racine R., 1991, AJ, 102, 454
 Rix H. W., Schneider D. P., Bahcall J. N., 1992, AJ, 104, 959
 Schmidt R. W., 1996, Master thesis, University of Melbourne
 Schneider D. P., Turner E. L., Gunn J. E., Hewitt J. N., Schmidt M., Lawrence C. R., 1988, AJ, 95, 1619; Erratum, 1988, AJ, 96, 1755
 Schneider P., Ehlers J., Falco E. E., 1992, "Gravitational Lenses", Springer Verlag, Berlin
 Schramm T., 1990, A&A, 231, 19
 Schramm T., 1994, A&A, 284, 44
 Sellwood J., Wilkinson A., 1993, Rep. Prog. Phys., 56, 173
 Tyson J. A., Gorenstein M. V., 1985, Sky & Telescope, 70, 319
 Walsh D., Carswell R. F., Weymann R. J., 1979, Nature, 279, 381
 Wambsganss J., Paczyński B., 1992, ApJ, 397, L1
 Wambsganss J., Paczyński B., 1994, AJ, 108, 1156
 Westphal J., 1992, HST proposal ID 3799
 Witt H. J., Mao S., 1994, ApJ, 429, 66
 Witt H. J., Mao S., Schechter P. L., 1995, ApJ, 443, 18
 Witt H. J., 1996, ApJ, 472, L1
 Witt H. J., Mao S., 1997, ApJ, accepted
 Yee H. K. C., 1988, AJ, 95, 1331

APPENDIX A: POWER-LAW ELLIPTICAL MASS DISTRIBUTIONS

The lensing properties of the elliptical power-law mass distributions from Equation (2) with $\nu = 1$ have been described by Kassiola & Kovner (1993) and Kormann, Schneider, & Bartelmann (1994). Kormann *et al.* determined these by solving the Poisson equation for the deflection potential ψ (see Schneider *et al.* 1992 for the definition of the deflection potential) in polar coordinates $\theta = \sqrt{\theta_1^2 + \theta_2^2}$ and φ

$$\frac{1}{\theta} \frac{\partial}{\partial \theta} \left(\theta \frac{\partial \psi}{\partial \theta} \right) + \frac{1}{\theta^2} \frac{\partial^2 \psi}{\partial \varphi^2} = 2\kappa(\theta, \varphi). \quad (\text{A1})$$

Their approach can be generalised for arbitrary real numbers ν with $0 \leq \nu < 2$. Define $n = 2 - \nu$, $s_n = \sin n \frac{\pi}{2}$, $c_n = \cos n \frac{\pi}{2}$ and

$$\Delta(\varphi) = \sqrt{\frac{\cos^2 \varphi}{(1 + \epsilon)^2} + \frac{\sin^2 \varphi}{(1 - \epsilon)^2}}. \quad (\text{A2})$$

Using the integrals

$$\begin{aligned} \mathcal{N}_1 &= \int_0^\varphi \frac{\cos n \varphi'}{\Delta^\nu(\varphi')} d\varphi' \\ \mathcal{N}_2 &= \int_\varphi^{\frac{\pi}{2}} \frac{\sin n \varphi'}{\Delta^\nu(\varphi')} d\varphi' \end{aligned}$$

$$\mathcal{N}_3 = \mathcal{N}_1 + \int_{\varphi}^{\frac{\pi}{2}} \frac{\cos n\varphi'}{\Delta^{\nu}(\varphi')} d\varphi', \quad (\text{A3})$$

the deflection potential for $0 \leq \varphi \leq \frac{\pi}{2}$ is given by

$$\psi(\theta, \varphi) = E_0 \theta^n \left[\frac{1}{n} \mathcal{N}_1 \sin n\varphi + \frac{1}{n} \left(\mathcal{N}_2 + \frac{c_n}{s_n} \mathcal{N}_3 \right) \cos n\varphi \right]. \quad (\text{A4})$$

The potential for the other quadrants can be taken from this result because of the elliptical symmetry of the mass distribution. The deflection angles $\vec{\alpha} = \vec{\nabla}\psi$ for this quadrant can be calculated from Equation (A4). The cartesian components are

$$\begin{aligned} \alpha_1(\theta, \varphi) &= E_0 \theta^{n-1} \left[\mathcal{N}_1 \left(\sin n\varphi \cos \varphi - \cos n\varphi \sin \varphi \right) \right. \\ &\quad \left. + \left(\mathcal{N}_2 + \frac{c_n}{s_n} \mathcal{N}_3 \right) \left(\cos n\varphi \cos \varphi + \sin n\varphi \sin \varphi \right) \right] \\ \alpha_2(\theta, \varphi) &= E_0 \theta^{n-1} \left[\mathcal{N}_1 \left(\sin n\varphi \sin \varphi + \cos n\varphi \cos \varphi \right) \right. \\ &\quad \left. + \left(\mathcal{N}_2 + \frac{c_n}{s_n} \mathcal{N}_3 \right) \left(\cos n\varphi \sin \varphi - \sin n\varphi \cos \varphi \right) \right]. \quad (\text{A5}) \end{aligned}$$

These expressions can be evaluated numerically. For $\nu = n = 1$ the integrals are analytically solvable and the formulas become identical to the results by Kassiola & Kovner (1993) and Kormann *et al.* (1994). After this work was completed, we discovered that Grogin & Narayan (1996) also used power-law elliptical mass profiles in their model of the lens of the double quasar 0957+561. In their paper they present the deflection angles of power-law elliptical mass distributions in a complex-valued lensing formalism in terms of the complex hypergeometric function.

APPENDIX B: FERRERS PROFILES

The deflection potential ψ_0 and the deflection angles $\vec{\alpha}_0$ of an elliptical slice of constant surface density, a Ferrers profile from Equation (4) with $\lambda = 0$, are given by

$$\psi_0(\theta_1, \theta_2) = -\frac{1}{2} ab\kappa_c (Q_{00} - \theta_1^2 Q_{10} - \theta_2^2 Q_{01}) \quad (\text{B1})$$

and the cartesian components

$$\begin{aligned} \alpha_{01}(\theta_1, \theta_2) &= ab\kappa_c \theta_1 Q_{10} \\ \alpha_{02}(\theta_1, \theta_2) &= ab\kappa_c \theta_2 Q_{01}, \end{aligned} \quad (\text{B2})$$

where

$$\begin{aligned} Q_{00} &= 2 \ln \left(\sqrt{a^2 + \rho} + \sqrt{b^2 + \rho} \right)^{-1} \\ Q_{01} &= \frac{2}{a^2 - b^2} \left(\sqrt{\frac{a^2 + \rho}{b^2 + \rho}} - 1 \right) \\ Q_{10} &= 2/\Delta(\rho) - Q_{01}. \end{aligned} \quad (\text{B3})$$

ρ is the positive solution of

$$\frac{\theta_1^2}{a^2 + \rho} + \frac{\theta_2^2}{b^2 + \rho} = 1 \quad (\text{B4})$$

outside the bar, and $\rho = 0$ inside the bar. $\Delta(\rho)$ is given by

$$\Delta(\rho) = \sqrt{(a^2 + \rho)(b^2 + \rho)}. \quad (\text{B5})$$

$\vec{\alpha}_0$ has first been derived by Schramm (1990) by using the known force field for a homogenous ellipsoid and letting the

largest axis go to infinity in order to get the corresponding 2-dimensional equations. To derive the potential ψ_0 in terms of real-numbered coordinates θ_1, θ_2 , we applied Schramm's method to the results by Pfenniger (1984) for the potential and force fields of 3-dimensional Ferrers ellipsoids. This enables us to calculate deflection potential and deflection angles for a whole family of Ferrers profiles. The deflection potential for Ferrers surface-density profiles with integer exponents λ is given by

$$\psi_{\lambda}(\theta_1, \theta_2) = -\frac{ab\kappa_c}{2(\lambda+1)} \int_{\rho}^{\infty} \frac{du}{\Delta(u)} \left(1 - \frac{\theta_1^2}{a^2 + u} - \frac{\theta_2^2}{b^2 + u} \right)^{\lambda+1}. \quad (\text{B6})$$

The corresponding 3-dimensional expression was first derived by Ferrers (1877). For integers $j, k, j \neq 0$ or $k \neq 0$, this integral can be split up into a sum containing the coefficients

$$Q_{jk} = \int_{\rho}^{\infty} \frac{du}{\Delta(u)} \frac{1}{(a^2 + u)^j (b^2 + u)^k}. \quad (\text{B7})$$

For Q_{00} use Equation (B3); a remaining contribution from the infinite axis had to be subtracted here. Pfenniger (1984) solved his corresponding integrals using recurrence relations. Translated into two dimensions, the Q_{jk} obey the relation

$$Q_{jk} = (Q_{j-1,k} - Q_{j,k-1}) / (a^2 - b^2), \quad (\text{B8})$$

as well as for $n > 0$

$$Q_{n0} = \frac{1}{2n-1} \left[\frac{2}{\Delta(\rho)(a^2 + \rho)^{n-1}} - Q_{n-1,1} \right], \quad (\text{B9})$$

$$Q_{0n} = \frac{1}{2n-1} \left[\frac{2}{\Delta(\rho)(b^2 + \rho)^{n-1}} - Q_{1,n-1} \right]. \quad (\text{B10})$$

With these equations, the deflection potential ψ_{λ} as well as the deflection angles $\vec{\alpha}_{\lambda} = \vec{\nabla}\psi_{\lambda}$ can be calculated from Equation (B6). The coefficients Q_{ij} can be treated as constant for the derivation with respect to θ_1 and θ_2 since the definition of ρ in Equation (B4) implies that $\frac{\partial \psi_{\lambda}}{\partial \rho} = 0$.

This paper has been produced using the Royal Astronomical Society/Blackwell Science L^AT_EX style file.